Measuring the labeling efficiency of pseudocontinuous arterial spin labeling

Chen, Z.S.; Zhang, X.X.; Yuan, C.; Zhao, X.H.; Osch, M.J.P. van

Modular Transmit/Receive Arrays Using Very-High Permittivity Dielectric Resonator Antennas

Thomas P.A. O'Reilly, Thomas Ruytenberg, and Andrew G. Webb*

Purpose: Dielectric resonator antenna (DRAs) are compact structures that exhibit low coupling between adjacent elements and therefore can be used as MRI transmit arrays. In this study, we use very high permittivity materials to construct modular flexible transceive arrays of a variable numbers of elements for operation at 7T.

Methods: DRAs were constructed using rectangular blocks of ceramic (lead zirconate titanate, $\varepsilon_r = 1070$) with the transverse electric $(TE)_{01}$ mode tuned to 298 MHz. Finite-difference time-domain simulations were used to determine the B_1 and specific absorption rate distributions. B_1^+ maps were acquired in a phantom to validate the simulations. Performance was compared to an equally sized surface coil. In vivo images were acquired of the wrist (four elements), ankle (seven elements), and calf muscle (16 elements).

Results: Coupling between DRAs spaced 5 mm apart on a phantom was −18.2 dB compared to −9.1 dB for equivalently spaced surface coils. DRAs showed a higher B_1^+ intensity close to the antenna but a lower penetration depth compared to the surface coil.

Conclusion: DRAs show very low coupling compared to equally sized surface coils and can be used in transceive arrays without requiring decoupling networks. The penetration depth of the current DRA geometry means they are ideally suited to imaging of extremities. **Magn Reson Med 79:1781–1788, 2018.**

Key words: high permittivity materials; dielectric resonator antenna; high field magnetic resonance; extremity imaging; enhanced decoupling

INTRODUCTION

Ultrahigh field (UHF) MRI suffers from B_1 inhomogeneities due to radiofrequency (RF) interferences that arise when the RF wavelength is of the same order as the imaging region of interest (1,2). It has been shown that B_1^+ inhomogeneities can be reduced through use of multi-element transmit array systems (3). Although receive-only arrays universally are used in UHF, MRI transmit arrays predominantly are used for body imaging using decoupled surface coils (4); microstrip or dipole antenna (5,6); and to a lesser extent, neuroimaging using decoupled surface coils[7] or an array of decoupled transmission line antenna (8,9). Musculoskeletal (MSK) imaging is less sensitive to B_1^+ inhomogeneities due to the relatively small dimensions of the typical region of interest; as a result, the birdcage remains the dominant design for RF transmission (10–12). Nevertheless, recent studies have begun to show the utility of transmit arrays for MSK imaging at 7T (13–16). Array designs utilizing overlapping surface coils—with the surface coils either fixed on a cylindrical housing into which the region of interest (ROI) is inserted (16), or with two separate surface coil arrays that are placed around the ROI (13,14)—have shown promise. An innovative *U*-shaped eight-channel microstrip array using capacitive decoupling has been used for imaging the ankle joint at 7T (15).

One of the main issues in designing large multi-element arrays is RF coupling between proximal array elements (17). Aside from causing changes in the impedance of individual array elements, RF coupling also reduces the signal-to-noise ratio (SNR) in parallel imaging techniques (18,19). Many system designs have been proposed to reduce inter-element coupling, including the overlapping of surface coils, preamplifier decoupling (18), resonant inductive decoupling (20), capacitive decoupling (21), inductive decoupling (22), decoupling annexes (23), and induced current elimination (24). The implementation of these systems typically increases the complexity of the antenna arrays. Decoupling methods that introduce additional decoupling structures to the array, such as the aforementioned resonant inductive decoupling and induced current elimination methods, are highly sensitive to geometric changes to the decoupling structures and subsequently to array deformation. Changes in coil loading also can impact the effectivity of decoupling systems (20) and change the inductance/capacitance value needed for optimal decoupling of array elements (25). Furthermore, the introduction of additional decoupling elements can result in significant alterations to the B_1^+ distribution compared to independent antenna (26).

High permittivity materials (also referred to as dielectric materials in other literature) have seen increased usage as the trend toward higher magnetic fields continues. High-permittivity pads placed between the patient and the transmit coil have been used to tailor B_1^+ fields, with the aim to improving B_1^+ homogeneity in body- and

C.J. Gorter Center for High Field MRI, Department of Radiology, Leiden University Medical Center, Leiden, The Netherlands.

Grant sponsor: This work was funded by the NWO-STW, grant number 13783.

*Correspondence to: Andrew Webb, C.J. Gorter Center for High Field MRI, Department of Radiology, Leiden University Medical Center, Albinusdreef 2, 2333 ZA Leiden, Netherlands. E-mail: a.webb@lumc.nl.

Received 25 January 2017; revised 25 April 2017; accepted 17 May 2017
DOI 10.1002/mrm.26784
Published online 20 June 2017 in Wiley Online Library (wileyonlinelibrary.com).

neuroimaging at high field (27–30) and neuroimaging in ultrahigh field MRI (31,32), or for strong local focusing of B_1^+ to improve signal intensity in the cervical spine at 3T (30) and in the inner ear at 7T (33). The interesting electromagnetic (EM) properties of high-permittivity materials (HPMs) have seen them integrated into several (UHF) antenna designs. The shortened RF wavelength in HPMs has been exploited to reduce the dimensions of bow-tie antenna by submerging them in water (34) and to construct dielectric waveguide antenna (35), again using water as the HPM. HPMs also have been used as substrates for dipole antenna to improve B_1^+ penetration and reduce specific absorption rate (SAR) (36,37).

Recent work has shown that dielectric resonator antenna (DRAs) operating in the transverse electric $(TE)_{01\delta}$ mode (38,39) and hybrid electromagnetic $(HEM)_{11\delta}$ (40) can be used as transceive antenna in ultrahigh field MRI. The frequency of the $TE_{01\delta}$ mode in the dielectric resonator used in DRAs is determined by the shape, dimensions, and relative permittivity of the material. No expression for the mode frequencies of rectangular dielectric resonators exist, and electromagnetic simulations typically are used to determine the exact design parameters. Both Lu et al. (38) and Aussenhofer and Webb (39) use cylindrical dielectric resonators constructed from water ($\varepsilon_r = 80$) and barium titanate ($\varepsilon_r = 170$), respectively. Although having several advantages compared to equivalently sized surface coils, including much lower interelement coupling (the electric field in the $TE_{01\delta}$ mostly is contained within the DRA; and the magnetic field mainly is in the z-direction, resulting in little EM interaction with adjacent elements), the individual elements reported in both papers were relatively large and correspondingly heavy, which impacts patient comfort in the scanner when used as surface elements.

In this paper, we present a new design of DRAs using rectangular elements with very high relative permittivities ($\varepsilon_r \sim 1070$), which result in much smaller and lighter antennas, thereby improving patient comfort compared to previous designs. The new lightweight DRAs, combined with the lack of need for decoupling networks, enable the construction of a flexible array with an arbitrary number of antennas that can be placed directly on the patient and conform to the particular region of interest. In vivo results are shown from scans using between four and 16 separate elements.

METHODS

Electromagnetic Simulations

EM simulations of the B_1 and SAR distributions of the DRAs were performed using the time-domain solver in CST Microwave Studio 2016 (CST AG, Darmstadt, Germany). A mesh size of 50 cells per wavelength was used for all simulations with open boundaries spaced $\lambda/10$ away from the model. The dielectric resonators were simulated with a relative permittivity of 1,070 and a conductivity of 1.5 S/m. A cuboid $120 \times 120 \times 210\,mm^3$ phantom ($\varepsilon_r = 80$, $\sigma = 0.40$ S/m) was used in all simulations. The SAR distribution was computed in accordance to the Institute of Electrical and Electronics Engineers Standards Association/International Electrotechnical Commission 62704-1 standard (41). All simulations were normalized to 1W accepted power. The intrinsic signal-to-noise ratio of the coils was evaluated using the method specified by Schnell et al. (42). The power loss in the phantom and antenna was determined using the same simulation method as for the B_1 and SAR.

Dielectric Resonator Construction

Rectangular ceramic blocks (TRS Technologies, State College, Pennsylvania, USA) with dimensions of $68 \times 90 \times 5\,mm^3$ were formed from sintered lead zirconate titanate (PZT). EM simulations using an eigenmode solver (CST Microwave Studio 2014, CST AG) were used to confirm the relative permittivity of the material by simulating the frequency of the $TE_{01\delta}$ mode for different permittivity values, and then comparing this with an S_{11} measurement using an unmatched 1-cm diameter pickup loop placed above the center of the ceramic block and a vector network analyzer (Planar TR1300/1, Copper Mountain Technologies, Indianapolis, Indiana, USA). The conductivity of the dielectric resonators was determined using a quality (Q)-factor measurement of the resonance peak. The relative permittivity value of 1,070 subsequently was used to determine the dimensions ($44 \times 90 \times 5\,mm^3$) of the ceramic block such that the $TE_{01\delta}$ mode was at 298 MHz. The ceramic block was trimmed to these dimensions, and the resonance frequency was experimentally measured to be 298 MHz using the unmatched loop.

Dielectric Resonator Antenna Design

An inductively coupled circular loop, with an inner diameter of 11 mm, an outer diameter of 15 mm, and a balanced matching network was constructed (see Fig. 1). The loop was placed concentrically above the DR to most effectively couple to the magnetic component of the $TE_{01\delta}$ mode of the DR. The distance between the loop and the DR to achieve critical coupling was determined. The distance between the loop and the DR was kept constant with a hard plastic separator. Impedance matching of the critically coupled system was performed with the DR placed on a $120 \times 120 \times 210\,mm^3$ saline phantom ($\varepsilon_r = 80$, $\sigma = 0.4$ S/m). The coupling between two DRAs placed next to one another was measured using the S_{12} parameter, with the long sides of the elements parallel to one another and placed on one face of a cuboid $120 \times 120 \times 210\,mm^3$ phantom ($\varepsilon_r = 80$, $\sigma = 0.4$ S/m).

Reference Surface Coil

Two rectangular surface coils with a balanced matching network, four tuning capacitors, outer dimensions of $90 \times 44\,mm^2$, and a copper trace width of 5 mm were constructed (see Fig. 1) as reference coils to compare performance with the DRs. The coils were tuned to 298 MHz and impedance matched to 50 Ω on a $120 \times 120 \times 210\,mm^3$ saline phantom ($\varepsilon_r = 80$, $\sigma = 0.4$ S/m). The coupling between the adjacent loops was measured using the same setup as for the DRAs.

MRI Data Acquisition

All experiments were performed on a 7T whole-body human MRI scanner (Phillips Achieva, Best, the Netherlands). All in vivo scans were performed on healthy volunteers, and

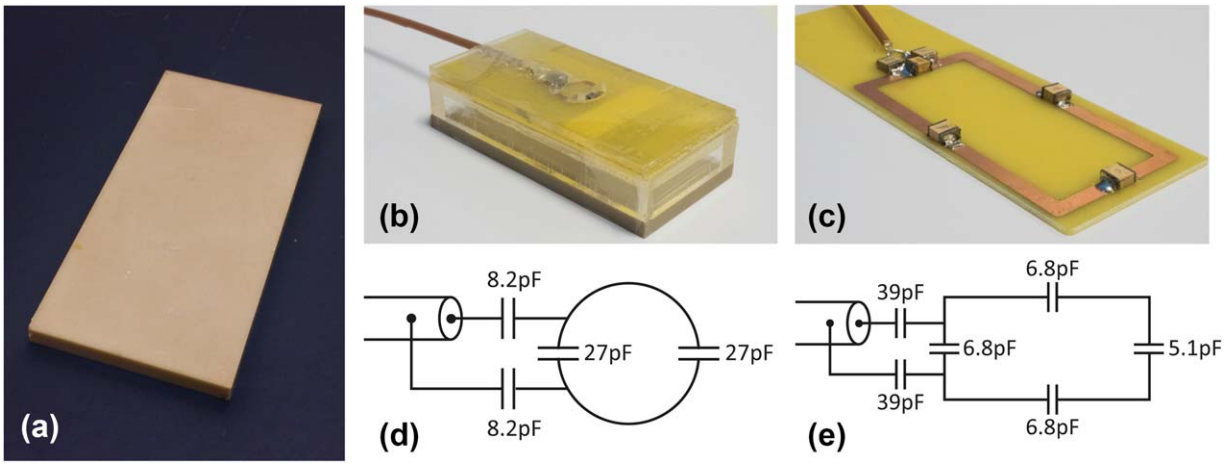

FIG. 1. (**a**) Dielectric resonator made from PZT with a relative permittivity of ~1,070. The dimensions of the block are $90 \times 44 \times 5\,mm^3$, such that the frequency of the $TE_{01\delta}$ mode is at 298 MHz. (**b**) A single DRA, the resonant loop is spaced 13 mm from the resonator. This distance is kept constant with a hard plastic separator. (**c**) Surface loop coil used for comparison to the DRAs. The outer dimensions are 90×44 mm, with a track width of 5 mm. (**d** and **e**) Circuit diagrams for the two loop coils.

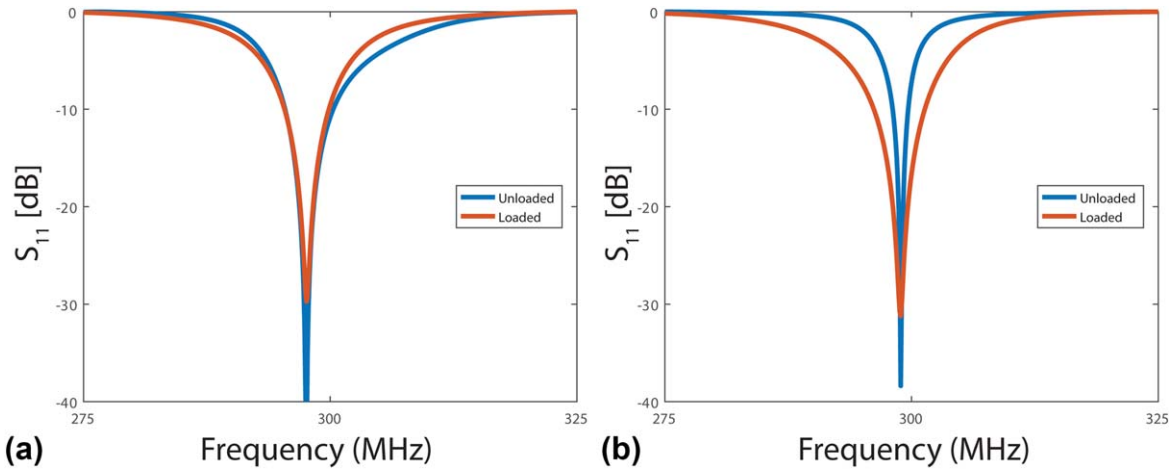

FIG. 2. Plot of the measured S_{11} parameters of (**a**) a dielectric resonator and (**b**) an equally sized surface coil, both unloaded and loaded with a human leg when the dielectric resonator and surface coil are critically coupled to a tuned 15-mm diameter resonant loop.

written consent was obtained from all volunteers prior to scanning. For experiments with the four-element DRA array, two independent transceive channels were split into a total of four channels using two 1-to-2 Wilkinson transmission line power dividers. The four element DRA array was driven with a relative phase difference of 0°, 0°, 90°, and 90° between the antenna measured in a clockwise direction. For experiments performed with seven- and 16-element DRA arrays, a custom-built 16-channel transmit/receive interface box was used. The interface box consists of two 1-to-8 Wilkinson transmission line power dividers, fed with two independent transmit channels, and 16 transmit/receive (TR) switches that provide 16 independent receive channels. The seven element DRA array was driven with a relative phase difference of 0°, 0°, 0°, 0°, 90°, 90°, and 90° between the antenna measured in a clockwise direction. The 16-element DRA array was driven with no phase difference between the antenna.

Table 1
The Required Distance Between a 15-mm Diameter Tuned Resonant Loop and a Dielectric Resonator or Equally Sized Surface Coil and the Measured Q-Factor of the System at the Point of Critical Coupling.

Antenna		Critical Coupling Distance (mm)	Q-Factor
Dielectric resonator	Unloaded	16	34.0
	Loaded	13	37.2
Surface coil	Unloaded	40	99.4
	Loaded	4	34.7

Q-factor, quality factor.

Single-slice B_1^+ maps were obtained using the dual refocusing echo acquisition mode sequence (43) with the following parameters: field of view = 16.3×10 cm, slice thickness = 5 mm, spatial resolution = 1.56×1.56 mm, stimulated echo acquisition mode (STEAM) flip angle = 60°, imaging tip angle = 10°, TR/TE = 5/1.13 ms, number of signal averages = 256, and acquisition time = 136 s. T_1-weighted 3D gradient recalled echo (GRE) images of the wrist were acquired with four DRA elements with the

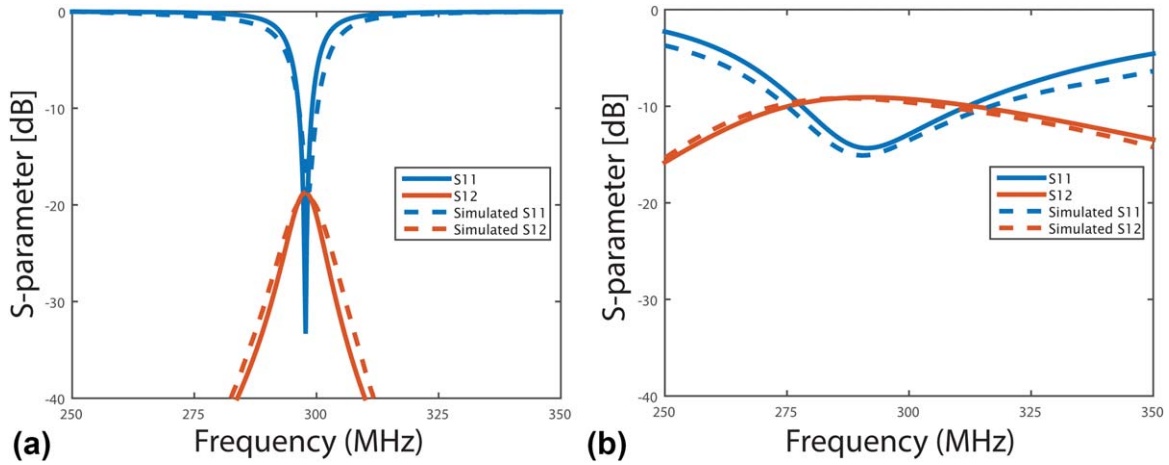

FIG. 3. Simulated (segmented line) and measured (solid line) S_{11} (blue) and S_{12} (orange) parameters of (**a**) two dielectric resonator antennae and (**b**) two surface coils spaced 5 mm apart on a phantom.

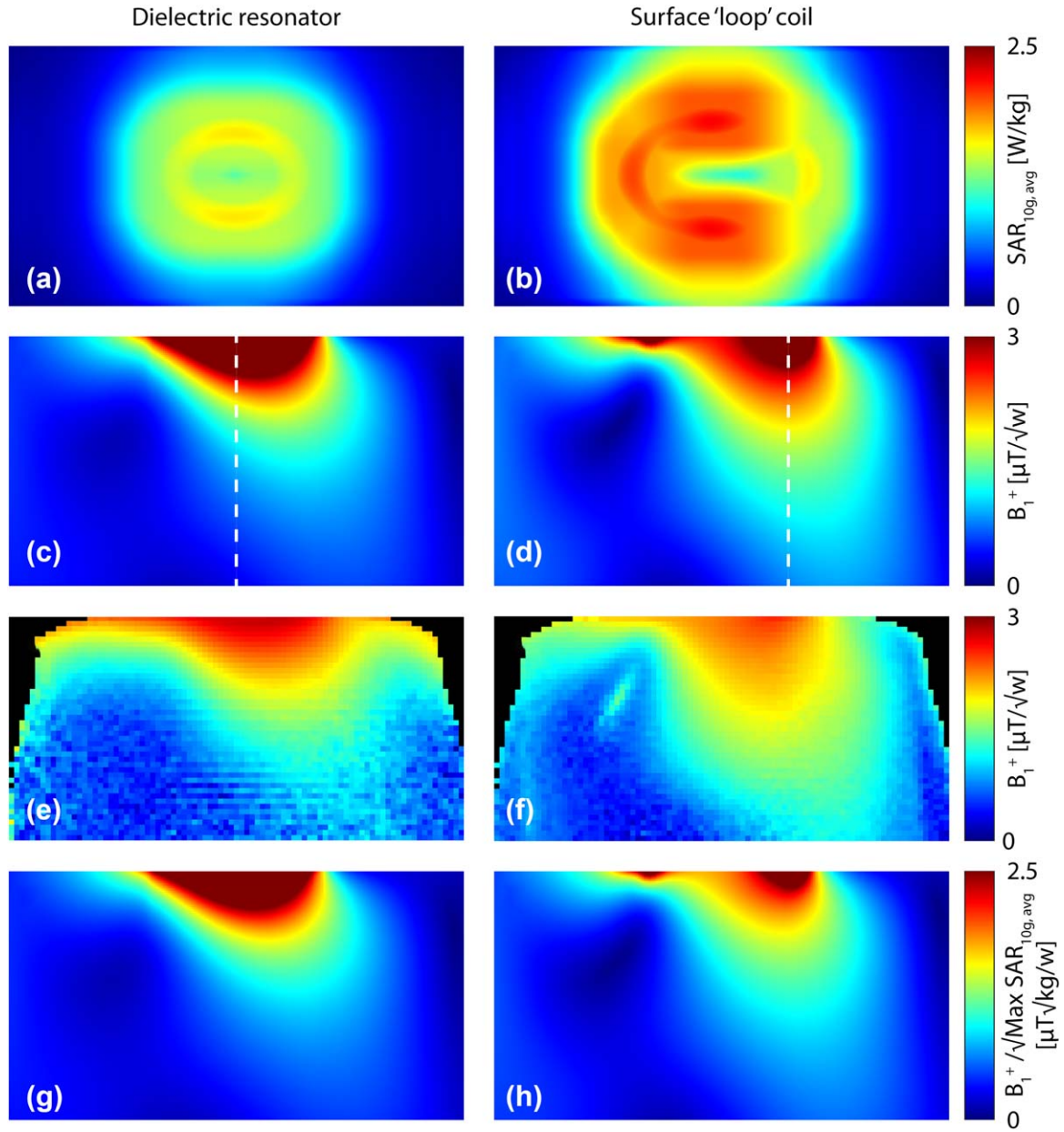

FIG. 4. (**a–b**) Maximum intensity plot of the simulated $SAR_{10g,\ avg}$ of the DRA and surface coil normalized to 1W input power placed on a $120 \times 120 \times 210\,mm^3$ phantom ($\varepsilon_r = 80$, $\sigma = 0.40$ S/m). (**c–d**) Simulated B_1^+ distribution normalized to 1W input power in the same phantom. (**e–f**) B_1^+ distribution measured using the dual refocusing echo acquisition mode sequence normalized to 1W input power. (**g–h**) Simulated B_1^+ distribution normalized to the maximum $SAR_{10g,\ avg}$, 1.62 W/kg, and 2.20 W/kg for the DRA and surface coil, respectively.DRA, dielectric resonator antenna; SAR, specific absorption rate.

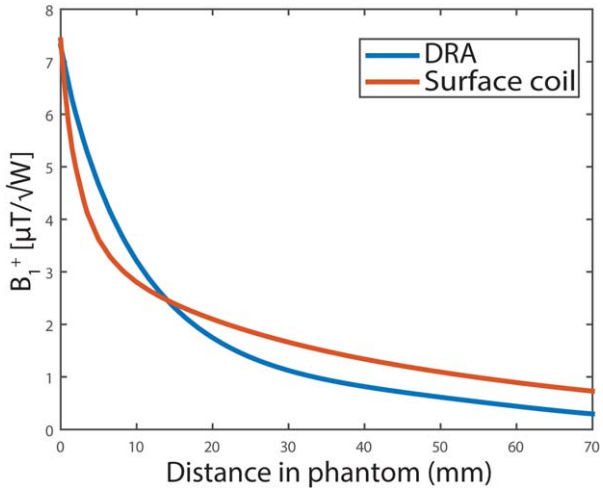

FIG. 5. Simulated B_1^+ per Watt accepted power for a dielectric resonator and a "loop" coil in a phantom. Both profiles were taking through each antenna's respective maximum B_1^+, indicated by a white line in Figures 4c and 4d.DRA, dielectric resonator antenna.

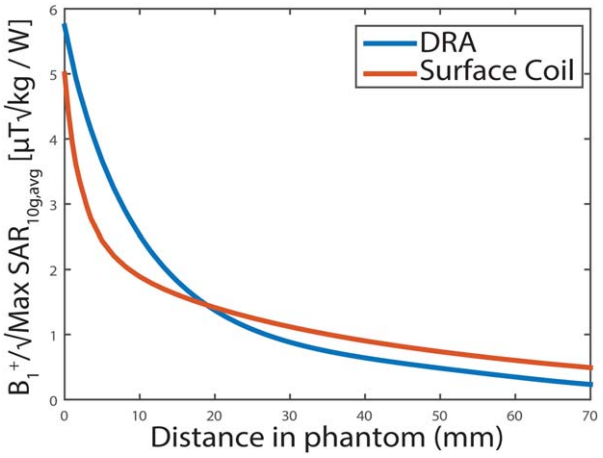

FIG. 6. Simulated B_1^+ profile normalized to maximum $SAR_{10g,\ avg}$ for a dielectric resonator and loop coil placed on a phantom ($120 \times 120 \times 210\,mm^3$, $\varepsilon_r = 80$, $\sigma = 0.40$ S/m).DRA, dielectric resonator antenna; SAR, specific absorption rate.

following parameters: field of view = $10 \times 10 \times 4$ cm, spatial resolution = $0.3 \times 0.3 \times 2$ mm, TR/TE = 20/3.2 ms, flip angle = 10°, echo train length = 30, and acquisition time- = 3m 18s. T_1-weighted 3D GRE images of the ankle were acquired with seven DRA elements, with the following parameters: field of view = $12 \times 12 \times 6$ cm, spatial resolution = $0.28 \times 0.28 \times 2$ mm, TR/TE = 20/3.2 ms, echo train length = 30, and acquisition time = 5m 37s. T_1-weighted 3D GRE images of the lower leg were acquired with 16 DRA elements, with the following parameters: field of view = $15 \times 15 \times 10$ cm, spatial resolution = $0.47 \times 0.47 \times 2$mm, TE/TR = 4.9/2.2 ms, flip angle = 20°, echo train length = 352, and acquisition time = 3m 28 s.

RESULTS

Coil Characterization

The reflection coefficient (S_{11} parameter) of all DRAs was measured to be lower than −30 dB, and that of the two reference surface coils less than −25 dB when loaded with a phantom. Figure 2 shows a plot of the S_{11} parameter of an unloaded dielectric resonator and surface coil, as well as the case when loaded with a human leg, using the same critically-coupled 15 mm diameter secondary loop. The separation distance at which critical coupling was achieved, as well as the Q-factor at the point of critical coupling, are reported in Table 1.

The interelement coupling (indicated by the S_{12} parameter) between two DRAs placed 5 mm apart on a phantom was −18.2 dB (see Fig. 3), with minimal change in S_{11} compared to the individual elements. Placing the DRAs directly against each other increases the coupling to −15.1 dB. The interelement coupling between the two surface coils separated by 5 mm is −9.1 dB (simulated) and −10.6 dB (measured), resulting in a shifted resonance frequency and reduced coil sensitivity. The simulated S-parameters of the DRA and surface coil show good agreement with measurements.

Electromagnetic Simulations

Maximum intensity plots of the 10-gram average SAR ($SAR_{10g,\ avg}$) of a DRA and surface coil are shown in Figure 4. The distribution of the $SAR_{10g,\ avg}$ of both

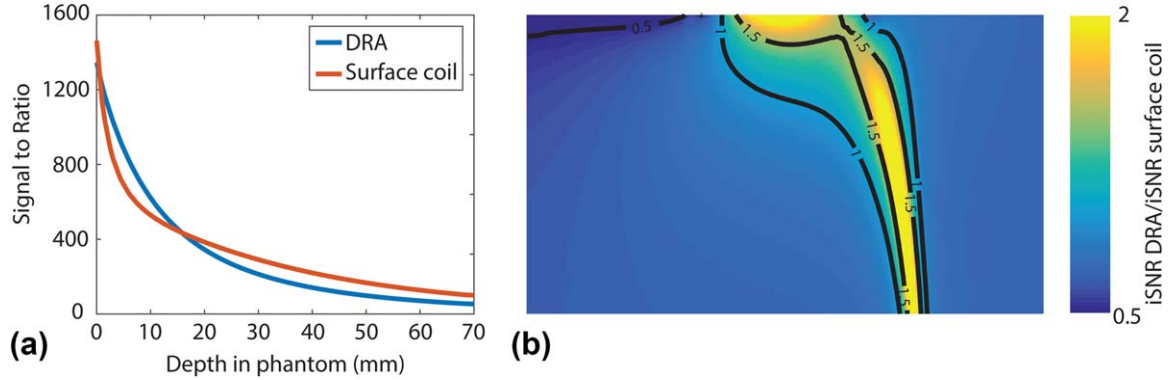

FIG. 7. (**a**) A profile of the intrinsic SNR for the DRA and surface coil placed on a phantom ($120 \times 120 \times 210\,mm^3$, $\varepsilon_r = 80$, $\sigma = 0.40$ S/m). (**b**) The ratio of the intrinsic SNR of the DRA and surface coil on the same phantom.DRA, dielectric resonator antenna; iSNR, intrinsic signal-to-noise ratio; SNR, signal-to-noise ratio.

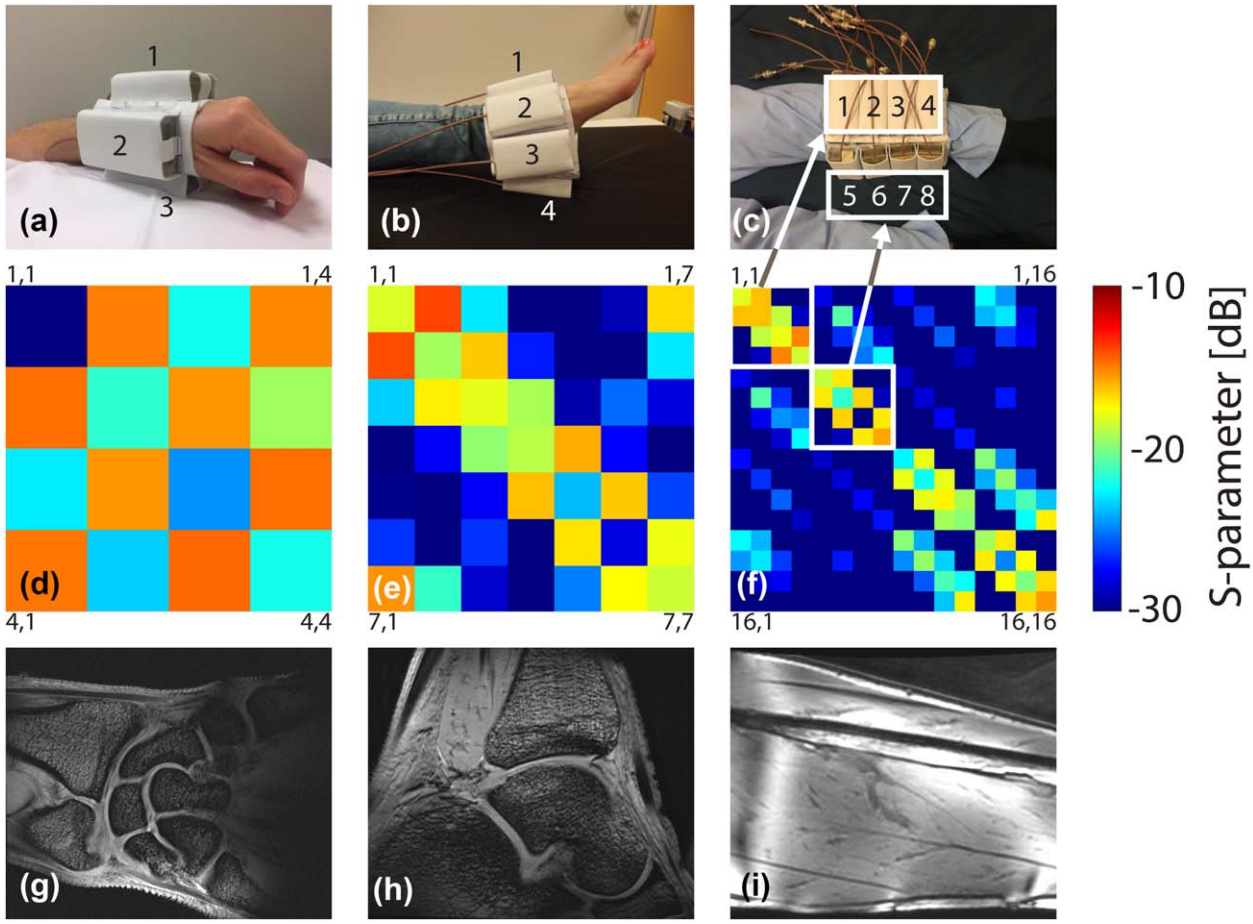

FIG. 8. (**a–c**) DRA array configuration for imaging the wrist (**a**,**d**,**g**), ankle (**b**,**e**,**h**) and calf muscle (**c**,**f**,**i**) using four, seven, and 16 elements. (**d–f**) S-parameter matrix of the respective configurations. (**g-i**) T_1-weighted 3D gradient recalled echo obtained using the DRA array as a transceive system.DRA, dielectric resonator antenna.

setups is similar, with the maximum SAR located proximally along the long side of the antenna/coil. The maximum $SAR_{10g,\ avg}$ of the DRA was 1.62 W/kg compared to a maximum $SAR_{10g,\ avg}$ of 2.20 W/kg for the surface coil. The simulated and measured B_1^+ distributions across the central slice of the antenna and the coil also are shown in Figure 4. There is good agreement between the simulated and measured B_1^+ distribution, although the very high B_1^+ close to the surface of both the DRA and surface coil is not replicated in the B_1^+ maps. This most likely is due to the limited dynamic range of the B_1^+ mapping method. The overall distribution of the B_1^+ is broadly similar between the DRA and surface coil, although the surface coil shows a slightly higher B_1^+ at greater depth.

Figure 5 shows the simulated B_1^+ along a line through the maximum B_1^+ of both antennas, marked by a segmented white line in Figures 4c and 4d for the DRA and surface coil, respectively. The DRA produces a stronger B_1^+ at shallow depths but has a stronger dropoff compared to the surface coil, with the latter displaying a higher B_1^+ at depths greater than 1.5 cm. Figure 6 shows the B_1^+ normalized to the maximum $SAR_{10g,\ avg}$, of the DRA and surface coil through the same lines as used in Figure 5. In this case, the crossover point is approximately 2 cm. Figure 7a shows a plot of the intrinsic SNR through the point of maximum intrinsic SNR for both the DRA and the surface coil. Figure 7b shows the ratio between the intrinsic SNR of the DRA and surface coil.

In Vivo Results

Figure 8 shows in vivo T_1-weighted 3D gradient echo images of a wrist, ankle, and lower leg with four, seven, and 16 DRA elements, respectively, as well as the S-parameter matrix measured for the various setups. Inter-element coupling did not exceed −14 dB in any of the configurations of the array. No retuning of the DRA array elements was required for the different imaging configurations. The S_{11} parameter was below −21 dB for all elements in the wrist array, −18 dB for all elements in the ankle array, and −15 dB for all elements in the leg array. Note that the configurations have not been extensively optimized, but the choice of the respective matrix (4×4, 7×1, 4×1) was made simply to show the versatility of placement of the resonators.

DISCUSSION

In this study, we have shown that lightweight DRAs consisting of extremely high permittivity materials can

be used to construct transceive surface arrays with arbitrary dimensions, without the need for additional decoupling systems due to the inherently high isolation of dielectric resonator antenna. The shape of the dielectric resonators was practical for the conformation of the DRA arrays to highly irregular body areas, but the small effective area of the $TE_{01\delta}$ mode contributes to the steep B_1^+ dropoff displayed by the DRAs compared to the equally sized surface coil. As such, this geometry is most suited for studying regions with relatively small dimensions or regions close to the surface of the body. Although this study has not optimized the shape of the dielectric resonators, we anticipate that significant optimizations in the B_1^+ distribution can be achieved by using square or circular resonators (field distribution of the TE_{01} mode would result in a larger fraction of the surface contributing to the B_1^+) as well as by using a larger dielectric resonator with lower relative permittivity. Furthermore, simulations indicate that a higher material conductivity is associated with a more "leaky" resonator, and both B_1 (magnetic fields) and SAR (electric fields) increase in magnitude with resonator conductivity, suggesting that transmit efficiency may be optimized at a particular (non-zero) resonator conductivity.

The PZT blocks are delivered in slabs with a predefined thickness and permittivity due to small interbatch variations in the permittivity ($\pm 5\%$); precise tuning of the resonators should only be done once their exact permittivity has been determined. PZT is a hard and brittle ceramic material with high lead content; therefore, cutting of the resonators should be done using specialized equipment, and waste products must be handled with care. It is interesting to note that PZT most commonly is used for wide-band ultrasound transducers; therefore, the conductivity of these types of materials tends to be high. However, it is certainly possible to produce materials with high relative permittivity and low conductivity, for example, materials used in dielectric resonators for MR microscopy (44), and this may lead to improved performance.

For the ceramic blocks used in our study, a change of ± 1 mm in the width, length, and thickness of the dielectric resonator results in a $\mp$ 3.3 MHz, ∓ 0.3 mm, and ∓ 23 MHz TE 01 mode frequency change, respectively. Because the resonators can be cut with millimeter accuracy, it is highly recommended to first cut the resonators to thickness and then cut the remaining dimensions.

Measurements of the temperature dependence of the relative permittivity of the dielectric resonators showed little variation, corresponding to a -0.3 MHz per degree temperature increase between 8°C and 65°C. No warming of the dielectric resonator was measured during the imaging in vivo imaging sequences; therefore, very minor changes in resonance frequency during imaging can be neglected.

CONCLUSION

In vivo imaging of the lower leg showed some image-intensity inhomogeneity. The inhomogeneities arise due to several factors: dielectric focusing due to the short RF wavelength in tissue; the fact that the coils are nonoverlapping, meaning they behave as spatially separated surface coils; and constructive and destructive interferences in the B_1^+ field of the individual array elements. This current study was performed using a system equipped with only two independent (in terms of transmit phase and amplitude) RF transmit channels, which severely limits the possibilities of B_1^+ shimming. Other groups have shown that significant improvements in B_1^+ homogeneity can be obtained through use of a higher number of independent transmit channels, and one can anticipate that the same will apply to DRA arrays.

REFERENCES

1. Hoult DI. Sensitivity and power deposition in a high-field imaging experiment. J Magn Reson Imaging 2000;12:46–67.
2. Ibrahim TS, Lee R, Abduljalil AM, Baertlein BA, Robitaille P-ML. Dielectric resonances and B1 field inhomogeneity in UHFMRI: computational analysis and experimental findings. Magn Reson Imaging 2001;19:219–226.
3. Vaughan JT, Snyder CJ, DelaBarre LJ, Bolan PJ, Tian J, Bolinger L, Adriany G, Andersen P, Strupp J, Ugurbil K. Whole-body imaging at 7T: preliminary results. Magn Reson Med 2009;61:244–248.
4. Zhao W, Cohen-Adad J, Polimeni JR, Keil B, Guerin B, Setsompop K, Serano P, Mareyam A, Hoecht P, Wald LL. Nineteen-channel receive array and four-channel transmit array coil for cervical spinal cord imaging at 7T. Magn Reson Med 2014;72:291–300.
5. Ipek O, Raaijmakers AJ, Klomp DW, Lagendijk JJ, Luijten PR, van den Berg CA. Characterization of transceive surface element designs for 7 Tesla magnetic resonance imaging of the prostate: radiative antenna and microstrip. Phys Med Biol 2012;57:343–355.
6. Ertürk MA, Raaijmakers AJE, Adriany G, Uğurbil K, Metzger GJ. A 16-channel combined loop-dipole transceiver array for 7 Tesla body MRI. Magn Reson Med 2017;77:884–894.
7. Gilbert KM, Belliveau J-G, Curtis AT, Gati JS, Klassen LM, Menon RS. A conformal transceive array for 7 T neuroimaging. Magn Reson Med 2012;67:1487–1496.
8. Adriany G, Auerbach EJ, Snyder CJ, Gözübüyük A, Moeller S, Ritter J, Van de Moortele P-F, Vaughan T, Uğurbil K. A 32-channel lattice transmission line array for parallel transmit and receive MRI at 7 Tesla. Magn Reson Med 2010;63:1478–1485.
9. Adriany G, Van de Moortele P-F, Ritter J, Moeller S, Auerbach EJ, Akgün C, Snyder CJ, Vaughan T, Uğurbil K. A geometrically adjustable 16-channel transmit/receive transmission line array for improved RF efficiency and parallel imaging performance at 7 Tesla. Magn Reson Med 2008;59:590–597.
10. Pakin SK, Cavalcanti C, La Rocca R, Schweitzer ME, Regatte RR. Ultra–high-field MRI of knee joint at 7.0T: preliminary experience. Acad Radiol 2006;13:1135–1142.
11. Regatte RR, Schweitzer ME. Ultra-high-field MRI of the musculoskeletal system at 7.0T. J Magn Reson Imaging 2007;25:262–269.
12. Chang G, Wiggins GC, Xia D, Lattanzi R, Madelin G, Raya JG, Finnerty M, Fujita H, Recht MP, Regatte RR. Comparison of a 28-channel receive array coil and quadrature volume coil for morphologic imaging and T2 mapping of knee cartilage at 7T. J Magn Reson Imaging 2012;35:441–448.
13. Kraff O, Bitz AK, Dammann P, Ladd SC, Ladd ME, Quick HH. An eight-channel transmit/receive multipurpose coil for musculoskeletal MR imaging at 7 T. Med Phys 2010;37:6368–6376.
14. Friedrich K, Chang G, Vieira R, Wang L, Wiggins G, Schweitzer M, Regatte R. In vivo 7.0-Tesla magnetic resonance imaging of the wrist and hand: technical aspects and applications. Semin Musculoskelet Radiol 2009;13:74–84.
15. Orzada S, Bitz AK, Schäfer LC, Ladd SC, Ladd ME, Maderwald S. Open design eight-channel transmit/receive coil for high-resolution and real-time ankle imaging at 7 T. Med Phys 2011;38:1162–1167.
16. Brown R, Madelin G, Lattanzi R, Chang G, Regatte RR, Sodickson DK, Wiggins GC. Design of a nested eight-channel sodium and four-channel proton coil for 7T knee imaging. Magn Reson Med 2013;70:259–268.
17. Lee RF, Giaquinto RO, Hardy CJ. Coupling and decoupling theory and its application to the MRI phased array. Magn Reson Med 2002; 48:203–213.
18. Roemer PB, Edelstein WA, Hayes CE, Souza SP, Mueller OM. The NMR phased array. Magn Reson Med 1990;16:192–225.

19. Pruessmann KP, Weiger M, Scheidegger MB, Boesiger P. SENSE: sensitivity encoding for fast MRI. Magn Reson Med 1999;42:952–962.
20. Avdievich NI, Pan JW, Hetherington HP. Resonant inductive decoupling (RID) for transceiver arrays to compensate for both reactive and resistive components of the mutual impedance. NMR Biomed 2013; 26:1547–1554.
21. Wu B, Zhang X, Qu P, Shen GX. Capacitively decoupled tunable loop microstrip (TLM) array at 7 T. Magn Reson Imaging 2007;25:418–424.
22. Bing W, Chunsheng W, Krug R, et al. 7T human spine imaging arrays with adjustable inductive decoupling. IEEE Trans Biomed Eng 2010; 57:397–403.
23. Kriegl R, Ginefri J-C, Poirier-Quinot M, Darrasse L, Goluch S, Kuehne A, Moser E, Laistler E. Novel inductive decoupling technique for flexible transceiver arrays of monolithic transmission line resonators. Magn Reson Med 2015;73:1669–1681.
24. Li Y, Xie Z, Pang Y, Vigneron D, Zhang X. ICE decoupling technique for RF coil array designs. Med Phys 2011;38:4086–4093.
25. Wu B, Zhang X, Qu P, Shen GX. Design of an inductively decoupled microstrip array at 9.4 T. J Magn Reson 2006;182:126–132.
26. Yan X, Gore JC, Grissom WA. New resonator geometries for ICE decoupling of loop arrays. J Magn Reson 2017;277:59–67.
27. Sreenivas A, Lowry M, Gibbs P, Pickles M, Turnbull LW. A simple solution for reducing artefacts due to conductive and dielectric effects in clinical magnetic resonance imaging at 3T. Eur J Radiol 2007;62:143–146.
28. de Heer P, Brink WM, Kooij BJ, Webb AG. Increasing signal homogeneity and image quality in abdominal imaging at 3 T with very high permittivity materials. Magn Reson Med 2012;68:1317–1324.
29. Sica C, Luo W, Rupprecht S, Lanagan M, Collins C, Sahul R, Kwon S, Yang Q. Ultra high dielectric constant (uHDC) head insert at 3T for dramatic reduction of SAR and B1 + inhomogeneity. In Proceedings of the 22nd Annual Meeting of ISMRM, Milan, Italy, 2014. p. 22.
30. Yang QX, Rupprecht S, Luo W, et al. Radiofrequency field enhancement with high dielectric constant (HDC) pads in a receive array coil at 3.0T. J Magn Reson Imaging 2013;38:435–440.
31. Snaar JE, Teeuwisse WM, Versluis MJ, van Buchem MA, Kan HE, Smith NB, Webb AG. Improvements in high-field localized MRS of the medial temporal lobe in humans using new deformable high-dielectric materials. NMR Biomed 2011;24:873–879.
32. Teeuwisse WM, Brink WM, Webb AG. Quantitative assessment of the effects of high-permittivity pads in 7 Tesla MRI of the brain. Magn Reson Med 2012;67:1285–1293.
33. Brink WM, van der Jagt AMA, Versluis MJ, Verbist BM, Webb AG. High permittivity dielectric pads improve high spatial resolution magnetic resonance imaging of the inner ear at 7 T. Invest Radiol 2014;49:271–277.
34. Winter L, Özerdem C, Hoffmann W, Santoro D, Müller A, Waiczies H, Seemann R, Graessl A, Wust P, Niendorf T. Design and evaluation of a hybrid radiofrequency applicator for magnetic resonance imaging and RF induced hyperthermia: electromagnetic field simulations up to 14.0 Tesla and proof-of-concept at 7.0 Tesla. PLoS ONEne 2013;8:e61661.
35. Bluemink JJ, Raaijmakers AJE, Koning W, Andreychenko A, Rivera DS, Luijten PR, Klomp DWJ, van den Berg CAT. Dielectric waveguides for ultrahigh field magnetic resonance imaging. Magn Reson Med 2016;76:1314–1324.
36. Ipek O, Raaijmakers A, Lagendijk J, Luijten P, van den Berg C. Optimization of the radiative antenna for 7-T magnetic resonance body imaging. Concepts Magn Reson Part B Magn Reson Eng 2013;43B:1–10.
37. Raaijmakers AJE, Ipek O, Klomp DWJ, Possanzini C, Harvey PR, Lagendijk JJW, van den Berg CAT. Design of a radiative surface coil array element at 7 T: the single-side adapted dipole antenna. Magn Reson Med 2011;66:1488–1497.
38. Lu JY, Zhang X, Rutt BK. A novel 7T transmit array using TE 01δ mode dielectric resonators. In Proceedings of the 21st Annual Meeting of ISMRM, Salt Lake City, Utah, USA, 2013. p. 21:4376.
39. Aussenhofer SA, Webb AG. An eight-channel transmit/receive array of TE01 mode high permittivity ceramic resonators for human imaging at 7 T. J Magn Reson 2014;243:122–129.
40. Aussenhofer SA, Webb AG. High-permittivity solid ceramic resonators for high-field human MRI. NMR Biomed 2013;26:1555–1561.
41. IEEE/IEC. Determining the peak spatial-average specific absorption rate (SAR) in the human body from wireless communications devices, 30 MHz–6 GHz.Part 1: general requirements for using the finite-difference time-domain (FDTD) method for SAR calculations. Volume P62704-12013.
42. Schnell W, Renz W, Vester M, Ermert H. Ultimate signal-to-noise-ratio of surface and body antennas for magnetic resonance imaging. IEEE Trans Antennas Propag 2000;48:418–428.
43. Nehrke K, Bornert P. DREAM—a novel approach for robust, ultrafast, multislice B(1) mapping. Magn Reson Med 2012;68:1517–1526.
44. Neuberger T, Tyagi V, Semouchkina E, Lanagan M, Baker A, Haines K, Webb AG. Design of a ceramic dielectric resonator for NMR microimaging at 14.1 Tesla. Concepts Magn Reson Part B Magn Reson Eng 2008;33B:109–114.